PAPER

Highly efficient and recyclable catalyst: porous Fe_3O_4–Au magnetic nanocomposites with tailored synthesis

To cite this article: Yichuan Kou *et al* 2020 *Nanotechnology* **31** 225701

IOP Publishing Nanotechnology
Nanotechnology 31 (2020) 225701 (12pp) https://doi.org/10.1088/1361-6528/ab767b

Highly efficient and recyclable catalyst: porous Fe_3O_4–Au magnetic nanocomposites with tailored synthesis

Yichuan Kou[1,2], Tong Wu[1,2], Guoliang Xing[3], Xiaohu Huang[4], Donglai Han[5], Shuo Yang[6], Chenzi Guo[6], Wei Gao[7], Jinghai Yang[1,2,9], Yang Liu[1,2,9] and Dandan Wang[8,9]

[1] College of Physics, Jilin Normal University, Siping 136000, People's Republic of China
[2] Key Laboratory of Functional Materials Physics and Chemistry of the Ministry of Education, Jilin Normal University, Changchun 130103, People's Republic of China
[3] Jilin Special Equipment Inspection and Research Institute, Jilin 132013, People's Republic of China
[4] Institute of Materials Research and Engineering, Agency for Science, Technology and Research, Singapore 138634, Singapore
[5] Engineering Research Center of Optoelectronic Functional Materials, Ministry of Education, Changchun 130022, People's Republic of China
[6] Changchun Institute of Optics, Fine Mechanics and Physics, Chinese Academy of Sciences, Changchun 130033, People's Republic of China
[7] School of Materials Science and Engineering, Jilin University, Changchun 130025, People's Republic of China
[8] GLOBALFOUNDRIES (Singapore) Pte. Ltd, 60 Woodlands Industrial Park D, Street 2, Singapore 738406, Singapore

E-mail: jhyang1@jlnu.edu.cn, liuyang@jlnu.edu.cn, ddwang1981@gmail.com and DANDAN.WANG@globalfoundries.com

Received 25 October 2019, revised 30 December 2019
Accepted for publication 14 February 2020
Published 13 March 2020

Abstract

In this work, we reported the tailored design of highly efficient Fe_3O_4–Au magnetic nanocomposite (MNP) catalysts. Fe_3O_4 nanocrystals with three different morphologies have been developed with engineered amounts of urea, and the plausible mechanism has been proposed. Then by controlling the amount of Au seeds, Fe_3O_4–Au MNPs with different morphologies and tunable Au deposition have been realized. Characterizations including x-ray diffraction (XRD), transmission electron microscopy (TEM), Mössbauer spectra, and elemental mapping are implemented to unveil the structural and physical characteristics of the successfully developed Fe_3O_4–Au MNPs with different morphologies. The catalytic ability of Fe_3O_4–Au MNPs with different morphologies have been compared by applying them to degrading RhB and 4-NP, meanwhile the correlation between the amount of Au seeds and the turnover frequency as well as the catalytic ability of Fe_3O_4–Au MNPs is investigated systematically. We found that the flower-like Fe_3O_4–Au MNPs with 20 ml Au seeds added achieved the best degradation efficiency of 96.7%, and their catalytic ability were almost unchanged after recycling. Out study sheds the light into the tailored design of highly efficient and recyclable catalysts for RhB and 4-NP.

Supplementary material for this article is available online

Keywords: Fe_3O_4 nanocrystals, Fe_3O_4–Au magnetic nanocomposites, morphology, formation mechanism, catalytic reduction

[9] Authors to whom any correspondence should be addressed.

(Some figures may appear in colour only in the online journal)

1. Introduction

Water pollution, aggravated by human activities is considered as one of the toughest issues as it poses a serious threat to environment and human health [1, 2]. Most notoriously, numerous organic dyes and nitroaromatic compounds have been discharged into aquatic environment with the overuse of industrial dyes, explosives and pesticides, and can potentially cause allergies, respiratory diseases, mutagenesis, loss of immunity, cancer, etc [3–6]. Therefore, the efficient degradation of industrial dyes and nitroaromatic compounds are urgently needed in recent years.

In the past years, various techniques, such as adsorption, photocatalysis and electrocatalysis, have been explored to solve the issue [7]. But they all failed to meet the needs of practical use, the adsorption technique is limited by the adsorption capacity of the adsorbents [8]; the photocatalysis suffers from slow reaction rate [9, 10]; while the electrocatalysis requires a large amount of energy [11].

Most recently, noble metal nanocrystals have risen as a promising solution to catalytic degradation because of their simple design, easy operation and high efficiency [12–14]. In particular, Au nanoparticles have been widely investigated due to their tunable optical properties and high catalytic activities [15]. Nevertheless, Au nanoparticles are prone to aggregating on account of their high surface energy, which leads to a decline in their active sites and hence results in their lower catalytic activities. Though suitable stabilizers could slightly suppress the aggregation of Au nanocrystals, but with the stabilizers covering the surface of Au nanocrystals, the catalytic activity of Au nanocrystals could be inhibited or even disabled [16–19]. Alternatively, to restrain the aggregation of Au nanoparticles, considerable efforts have been made in attaching Au nanoparticles onto solid supports, e.g. carbon, silica and magnetic materials [20]. Among all the choices, Fe_3O_4 magnetic nanocrystals received much attention, considering their high saturation magnetization, rapid reaction to outside magnetic fields and excellent biological compatibility. In our previous work, Fe_3O_4–Au microsphere nanocomposites were developed as recyclable catalysts for 4-nitrophenol (4-NP), which leaves pending discussions on improved morphologies of Fe_3O_4–Au nanocomposites. the morphology mechanism of relationship between the morphology of Fe_3O_4–Au nanocomposites and their catalytic performance [21, 22].

In this paper, Fe_3O_4–Au magnetic nanocomposites (MNP) with different morphologies have been investigated, the effect of the urea amount on the morphological properties of Fe_3O_4 nanocrystals was studied and a possible mechanism was proposed. By applying these Fe_3O_4–Au MNP and $NaBH_4$ in catalyzing rhodamine B (RhB) and 4-NP, we obtained the best morphology for Fe_3O_4–Au MNP catalysts and the most suitable amount of Au seeds for turnover frequency (TOF). We found that when degrading RhB and 4-NP, the flower-like Fe_3O_4–Au MNPs (adding 20 ml Au seeds) could achieve a stable conversion efficiency of 96.7%, and their catalytic performance was almost unchanged after magnetic recycling. Our study sheds light into the tailored design of recyclable highly efficient catalysts for reduction of RhB and 4-NP at the mass production level.

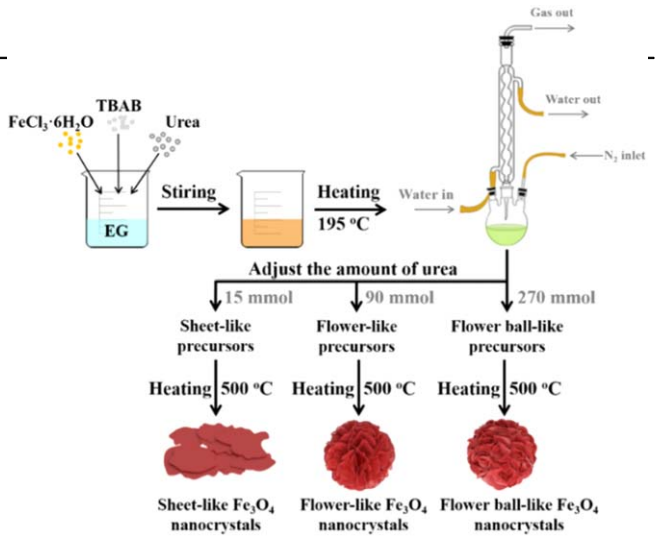

Scheme 1. Schematic diagram of the preparation process of Fe_3O_4 nanocrystals with different morphologies.

2. Experimental section

2.1. Synthesis of Fe_3O_4 nanocrystals with different morphologies

4.4 mmol of $FeCl_3·6H_2O$, 10.8 mmol of TBAB and urea (15, 90 and 270 mmol) were dissolved into 180 mL of EG by mechanical stirring respectively. Then transferred the mixtures to three-necked flasks and stirred with a magnetic stirrer for 20 min, respectively. Later the mixtures were refluxed at 190 °C in nitrogen flow for 18 min to remove the oxygen. During reaction, the mixtures gradually turned from colorless to yellow–green. The iron alkoxide precursors were obtained after cooling down to 25 °C naturally. Finally, the Fe_3O_4 nanocrystals were obtained by calcining the alkoxide precursors at 500 °C under N_2 atmosphere using a tube furnace. With 15, 90 and 270 mmol of urea added, sheet-like, flower-like and flower ball-like Fe_3O_4 nanocrystals were obtained respectively. The preparation process of Fe_3O_4 nanocrystals with different morphologies is shown in Scheme 1.

2.2. Synthesis of Au seeds

1 mL of 29 mM gold (III) chloride hydrate was placed into 90 mL of deionized water with vigorous stirring, followed by 6 mL of 1% $Na_3C_6H_5O_7·2H_2O$. After 1 min, 3 mL of 0.075% $NaBH_4$ was injected to the above mixture. After vigorous stirring for 15 h, Au seeds could be obtained.

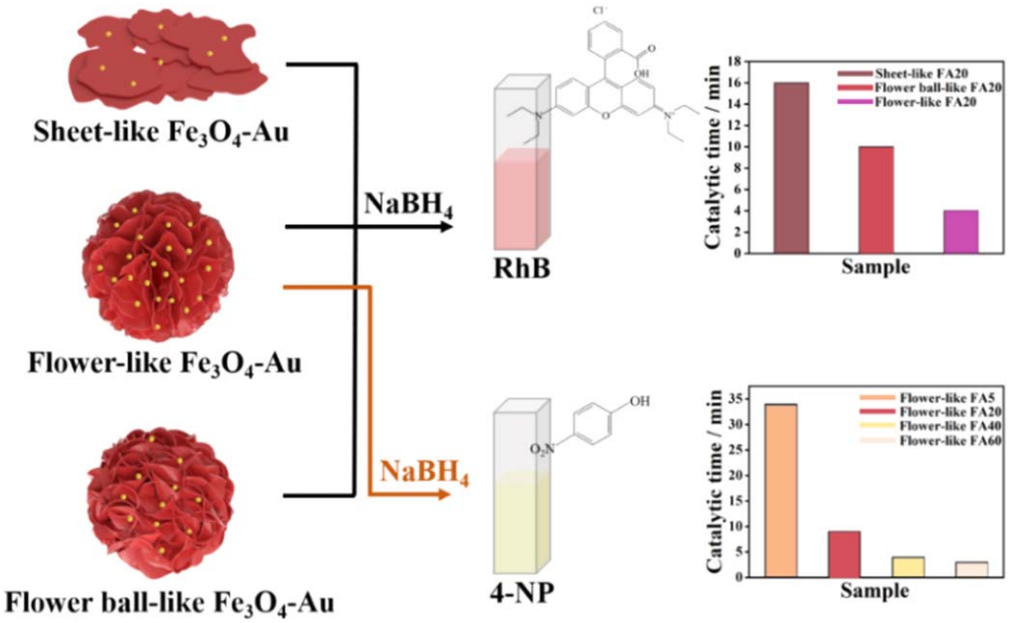

Scheme 2. Schematic illustration of catalytic reduction by Fe_3O_4–Au MNPs.

2.3. Synthesis of Fe_3O_4–Au MNPs

There were two steps to fabricate Fe_3O_4–Au MNPs: preparing Fe_3O_4@PEI-DTC and depositing Au seeds on the surfaces of Fe_3O_4@PEI-DTC. Fe_3O_4@PEI-DTC with different morphologies were prepared by the same method in our previous work and dispersed in 5 mL of deionized water, respectively [23]. Then 20 mL of the prepared Au seeds was added. After sonicating for 2 h, Fe_3O_4–Au MNPs were obtained by washing several times, named as sheet-like FA20, flower ball-like FA20, flower-like FA20, respectively. To evaluate the effect of Au seeds amount on structure and catalytic activity of flower-like Fe_3O_4@PEI-DTC nanoparticles, we adjusted the addition amount of Au seeds to 5 mL, 40 mL and 60 mL respectively, and obtained different Fe_3O_4–Au MNPs named as flower-like FA5, flower-like FA40, and flower-like FA60.

2.4. Fe_3O_4–Au MNPs for catalytic reduction of RhB and 4-NP

First, the catalytic performance of the as-prepared Fe_3O_4–Au MNPs on RhB (0.04 mM, 1 mL) and 4-NP (5 mM, 1 mL) was investigated. Second, to find out the best Fe_3O_4 nanocrystals morphology for attaching Au seeds, the catalytic reduction of RhB by Fe_3O_4–Au MNPs with different morphologies (sheet-like FA20, flower ball-like FA20, flower-like FA20) was compared. Third, to further uncover the effect of the Au seeds amount on the catalytic activities of Fe_3O_4–Au MNPs, the catalytic reduction of 4-NP by flower-like FA5, flower-like FA20, flower-like FA40 and flower-like FA60 (with different amounts of additional Au seeds) was compared. In a typical procedure, 0.1 mg of Fe_3O_4–Au MNPs and $NaBH_4$ (0.2 M, 1 mL) were added into the RhB and 4-NP, respectively. The reaction solution was detected by Ultraviolet-Visable (UV–vis) spectrophotometer every 120 s until it became colorless. The schematic illustration of the catalytic reduction by Fe_3O_4–Au MNPs is presented in Scheme 2. The sample was then separated by magnet for the recyclable use of Fe_3O_4–Au MNPs.

3. Results and discussion

The SEM images of the alkoxide precursors with different amounts of urea (15, 90 and 270 mmol) are shown in figure S1. It can be concluded that the amount of urea is crucial in shaping the morphology of the samples. If the amount of urea reaches to 15 mmol, the samples exhibit a thin sheet-like morphology. If the amount of urea increases to 90 mmol, the samples show a three-dimensional (3D) flower-like morphology with dense-layer petals. Once the amount of urea is increased to 270 mmol, the samples transform to 3D flower-ball nanostructures with curled petals. To help elucidate the process, we propose a possible formation mechanism of alkoxide precursors with different morphologies as follows: In cooperation with $FeCl_3$, EG acts as a linker and reductant to generate alkoxide precursors, which precipitates to get the primary nuclei [24] In this process, H^+ ions are released, which inhibits the generation of alkoxide precursors. But when urea is added into the p.recursor solution, it provides OH^- ions by urea hydrolysis and acts as an agent to neutralize the H^+ ions, which facilitates the generation of the alkoxide precursors [25]. With the increase of urea, the nucleus coarsens and aggregates into bigger nanoparticles and the 3D hierarchical nanostructures start to emerge with the self-assembly of nanoparticles. In the meantime, the petal surfaces of 3D hierarchical iron alkoxide precursors become glossy on account of Ostwald maturing. But if the amount of urea is no more than 15 mmol, the nanoparticles originating from iron alkoxide are insufficient to achieve the 3D

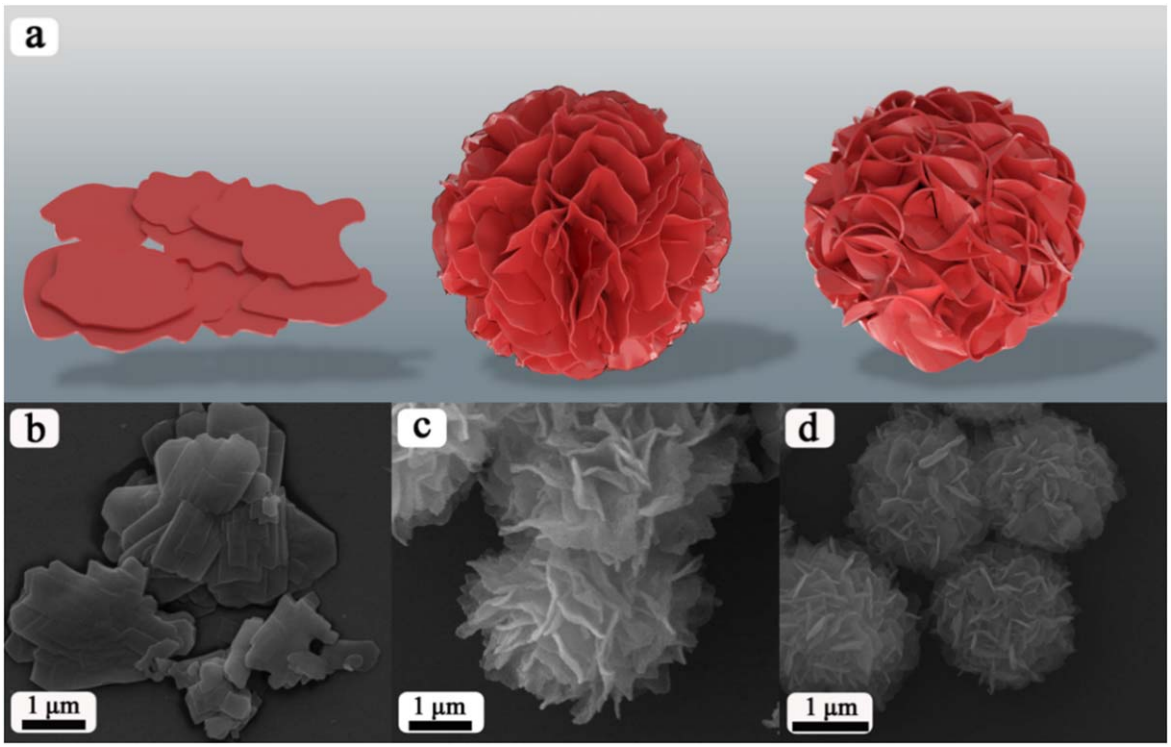

Figure 1. Simulated images (a) and the corresponding SEM images of sheet-like Fe_3O_4 nanocrystals (b), flower-like Fe_3O_4 nanocrystals (c) and flower ball-like Fe_3O_4 nanocrystals (d).

hierarchical nanostructures, which leaves us with the sheet-like nanostructures.

Figure 1 presents the simulated images and the corresponding SEM images of the Fe_3O_4 nanocrystals with different morphologies. Results show that the three samples maintain the original morphology, but close observation reveals that the alkoxide precursors changed from smooth and dense structure to polycrystalline and porous structure. The XRD patterns of Fe_3O_4 nanocrystals with different morphologies are shown in figure S2 is available online at stacks.iop.org/NANO/31/225701/mmedia.

The XRD patterns show that all the diffraction peaks of the three samples are indexed to the magnetite Fe_3O_4. No other impurities can be observed within the XRD detection limit. The peaks locate at about 30.4, 35.5, 43.4, 53.4, 57.3 and 62.8°, which can be attributed to the diffraction of Fe_3O_4 (JCPDS card no. 85–1436) [26, 27]. Since both Fe_3O_4 and γ-Fe_2O_3 have spinel structures and the difference between their cubic lattice constant is only 1%, it is not uneasy to distinguish them based on mere XRD results [28]. So Mössbauer spectra are further implemented to confirm the phase structure of flower-like Fe_3O_4 nanocrystals, as shown in figure S3. Two well-resolved sextets can be easily identified, and the strong lines of magnetic sextets exhibit a characteristic double six-peak structure of magnetite. One sextet owes to the Fe^{3+} ions at tetrahedral A-sites, and the other attributes to mixed valence Fe^{2+} and Fe^{3+} at octahedral B-sites [29]. Therefore, Mössbauer analyses further confirm that the flower-like Fe_3O_4 nanocrystals are single-phase Fe_3O_4 with cubic inverse-spinel structures [30].

The N_2 adsorption-desorption isotherm and the pore sizes of sheet-like, flower-like and flower ball-like Fe_3O_4 nanocrystals are presented in figure 2. Based on the Brunauer–Deming–Deming–Teller (BDDT) classification, the isotherms of the three samples exhibit the characteristics of type H3 hysteresis loops when the relative pressure is between 0.4 and 1.0, which demonstrates the presence of the mesopores in the three samples [31]. According to BJH method, the pore sizes range from 2 to 150 nm, as shown in the insets of figure 2. The BJH average pore sizes of sheet-like, flower-like and flower ball-like Fe_3O_4 nanocrystals are 9.49, 10.04 and 8.95 nm, respectively. The formation of the mesopores may be ascribed to the aggregation of the nanoparticles and the spaces between adjacent nanoparticles in the growth stage. In addition, the BET specific surface areas of sheet-likes, flower-like and flower ball-like Fe_3O_4 nanocrystals are 58.54, 60.73 and 59.25 $m^2\,g^{-1}$, respectively. The large specific surface area indicates that all three samples are promising solid supports.

XRD analyses were then again used to study the phase structures of Fe_3O_4–Au MNPs with different morphologies loaded with 20 ml Au seeds. As seen in figure 3, the XRD patterns show that other than the peaks of pure Fe_3O_4, there are four additional diffraction peaks 38.4, 44.5, 64.7 and 77.5°, which corresponds to the characteristic diffraction of Au [JCPDS 04–0784] and indicates the formation of Fe_3O_4–Au MNPs [16]. It is worth mentioning that the intensity of the Au diffraction peak of flower-like FA20 is higher than that of sheet-like FA20 and flower ball-like FA20. Since there is a direct ratio between the diffraction peaks and the contents of the phase, it can be expected that the surfaces

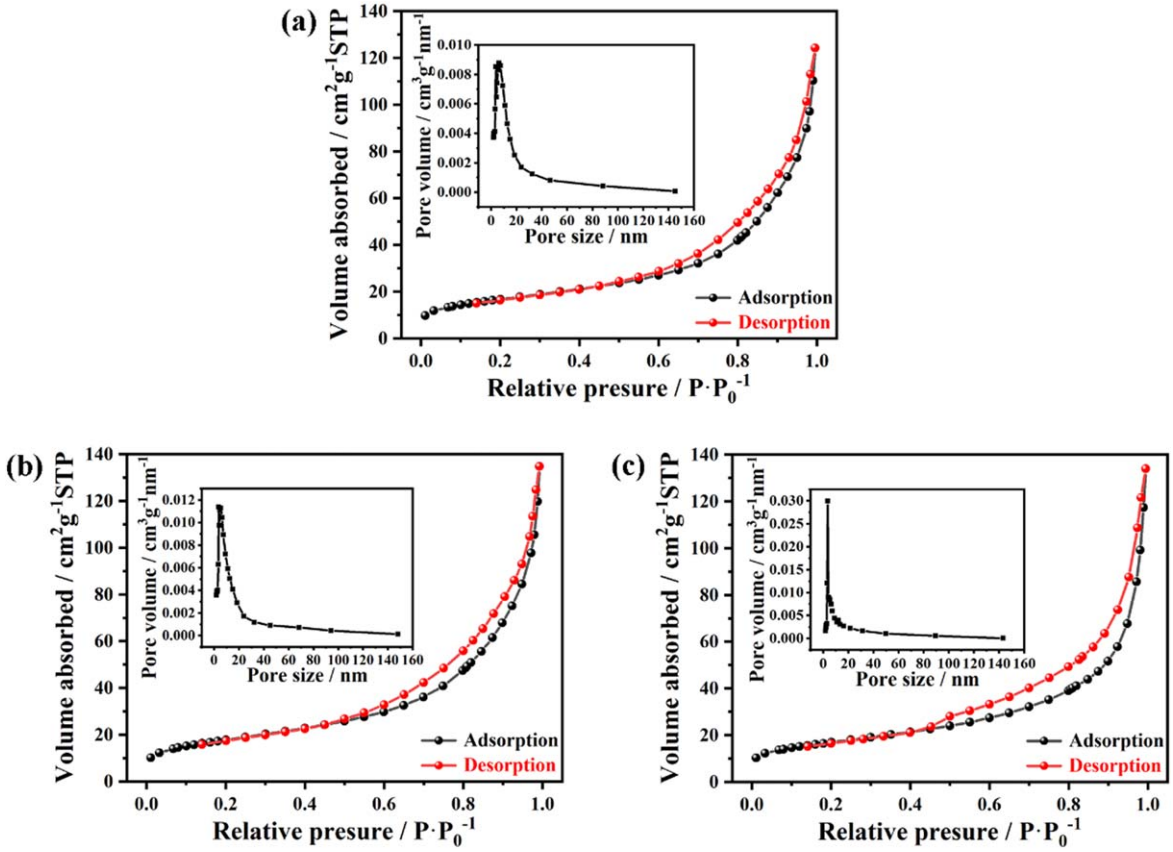

Figure 2. Nitrogen adsorption-desorption isotherms and the pore sizes (inset) of sheet-like (a), flower-like (b) and flower ball-like Fe_3O_4 nanocrystals (c).

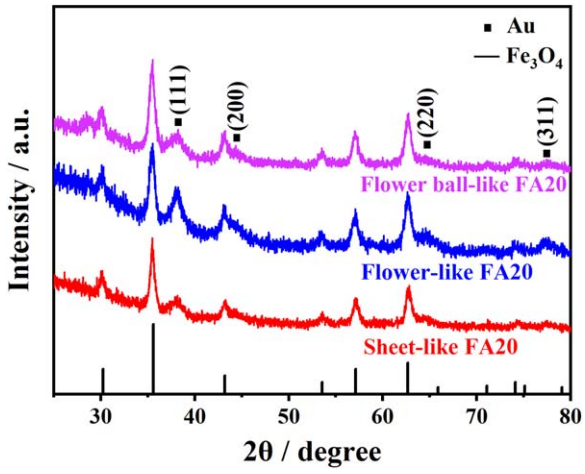

Figure 3. XRD patterns of sheet-like FA20, flower-like FA20 and flower ball-like FA20.

of flower-like FA20 have attached more Au seeds than those of sheet-like FA20 and flower ball-like FA20.

Figure 4 shows the TEM images of sheet-like FA20, flower-like FA20 and flower ball-like FA20. The high-resolution TEM (HRTEM) images in figures 4(c) and (e) show that the interplanar spacing of 0.253 and 0.236 nm matches with (311) plane of Fe_3O_4 and (111) plane of Au [16]. Selected area electron diffraction (SAED) patterns of sheet-like FA20, flower-like FA20 and flower ball-like FA20, as seen in figures 4(b), (d) and (f), consist of (220), (311), (400), (422), (511) and (440) diffraction rings of Fe_3O_4 and (111), (200) and (220) diffraction rings of Au, which further confirms the formation of the Fe_3O_4–Au MNPs [32]. The high-angle annular dark-field scanning TEM (HAADF-STEM) images and the corresponding energy-dispersive x-ray (EDS) elemental mapping images of the flower-like FA20 are shown in figure 4, from which we can observe an uniform deposition of Au seeds on the surface of Fe_3O_4 nanocrystals.

As shown in figure S4, the XPS scanning results indicate the existence of Fe, O, C and Au.

We can see from figure 5 that for the sheet-like FA20, Fe 2*p* XPS spectrum shows that the peaks locating at 711.7 and 725.8 eV are consistent with Fe $2p_{3/2}$ and $2p_{1/2}$; [33, 34] and the Au 4f spectrum presents that the peaks locating at 83.72 and 87.52 eV are consistent with $4f_{7/2}$ and $4f_{5/2}$ (caused by the split of spin–orbit) [35]. Notably, compared with the sheet-like FA20, Fe 2*p* peak positions of the flower-like FA20 shifts to lower binding energy and Au 4f peak locations of the flower-like FA20 move to higher binding energy, which may be explained by the strengthened electronic interaction between Au and Fe_3O_4 [23]. Another interesting finding is that the Au 4*f* peak intensity of the flower-like FA20 is higher than that of the sheet-like FA20 and the flower ball-like FA20. This can be possibly explained by the direct ratio between the XPS intensity and atomic concentration, which again implicates that the surfaces of flower-like FA20 have

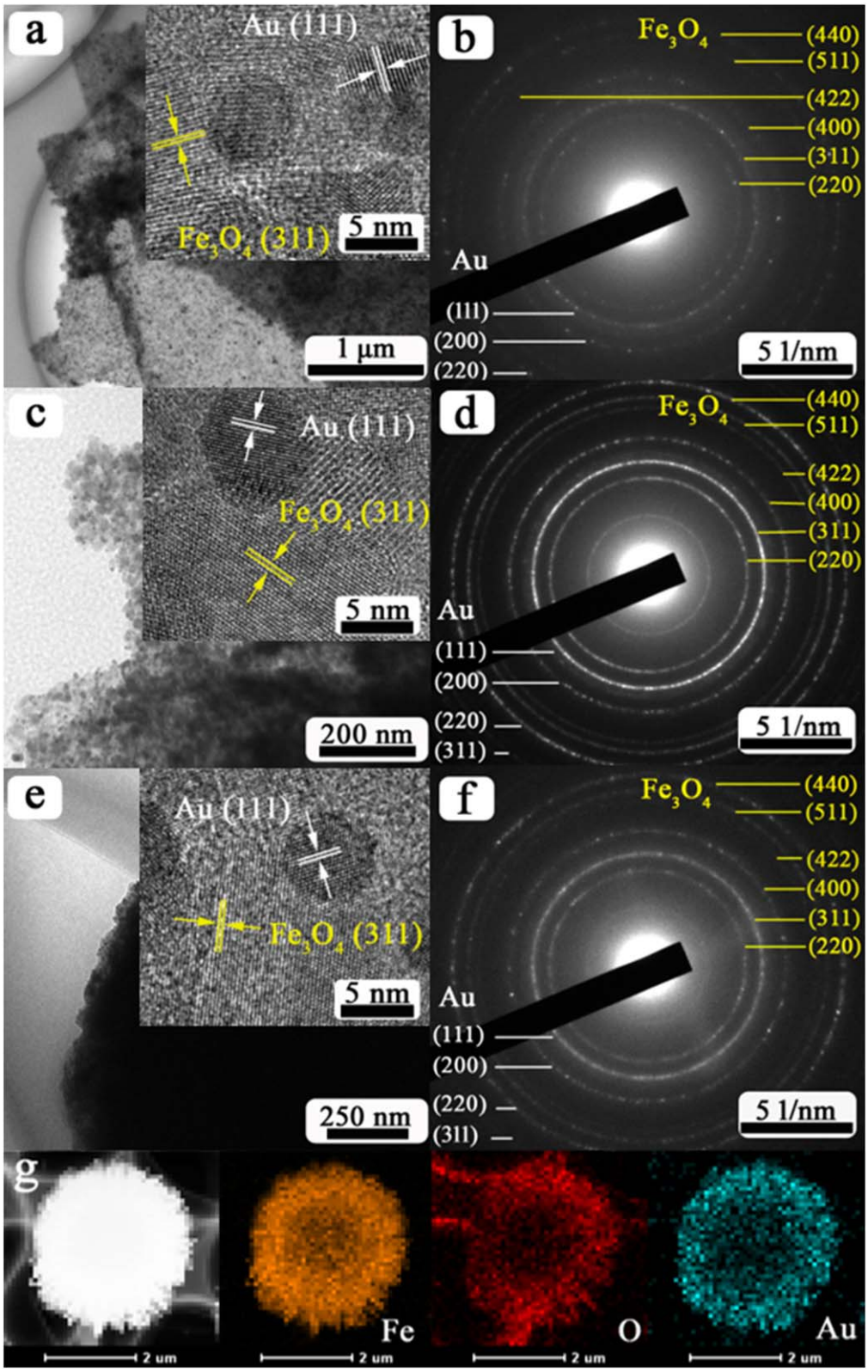

Figure 4. TEM images with HRTEM insets and SAED patterns of sheet-like FA20 ((a) and (b)), flower-like FA20 ((c) and (d)) and flower ball-like FA20 ((e) and (f)). HAADF-STEM images and the corresponding EDS elemental mapping images (Fe, O and Au) of flower-like FA20 (g).

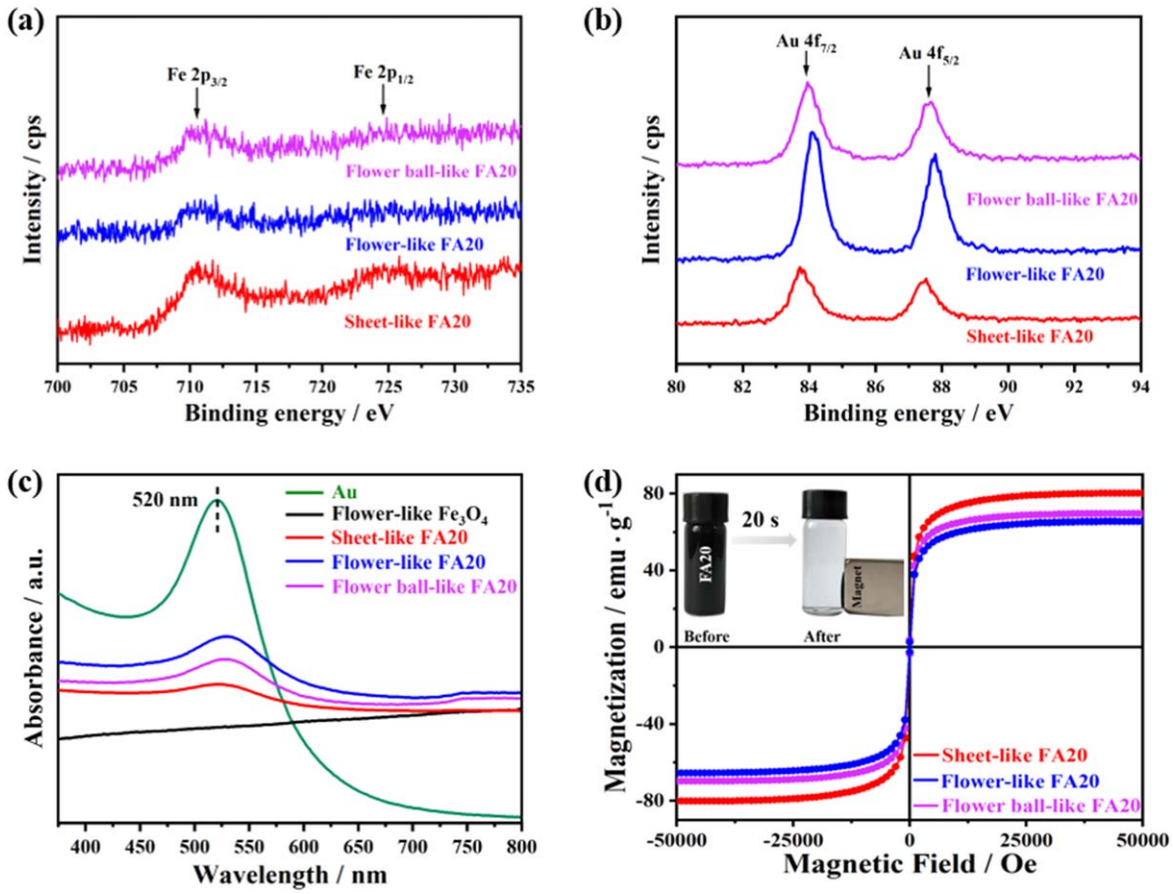

Figure 5. High-resolution XPS scans of Fe *2p* (a) and Au *4 f* (b) of sheet-like FA20, flower-like FA20 and flower ball-like FA20. UV–vis spectra (c) of Au seeds, flower-like Fe_3O_4 nanocrystals, sheet-like FA20, flower-like FA20 and flower ball-like FA20. Magnetic hysteresis (*M-H*) loops (d) of sheet-like FA20, flower-like FA20 and flower ball-like FA20. Inset of (d) shows the flower-like FA20 before and after magnetic separation.

attached more Au seeds than sheet-like FA20 and flower ball-like FA20 [36]. Figure 5(c) illustrates the UV–vis absorption spectra of Au seeds, flower-like Fe_3O_4 nanocrystals, sheet-like FA20, flower-like FA20 and flower ball-like FA20. The UV–vis spectrum of Au seeds exhibits a very intense plasmon absorption at 520 nm due to the energy coupling of free electron localized field and the collective oscillation [37, 38]. In comparison, the flower-like Fe_3O_4 nanocrystals exhibit no significant absorption peaks in the visible region. The SPR absorption peaks of the Fe_3O_4–Au MNPs show the characteristics of Au, only with red shifts. The observed red shifts are consistent with the demonstrated fact that the interfacial interaction between Au seeds and Fe_3O_4 nanocrystals could influence the position of surface plasmon absorption of Au [39–41]. Figure 5(d) shows the hysteresis loops of sheet-like FA20, flower-like FA20 and flower ball-like FA20 at 300 K. The saturation magnetization (*Ms*) values of sheet-like FA20, flower-like FA20 and flower ball-like FA20 are 80.1, 65.5 and 69.7 emu g^{-1}, respectively. We can see that the flower-like FA20 has the lowest Ms value. Since it has been known that the *Ms* values are in inverse proportion to the attached amount of Au seeds [42, 43], the magnetic results imply that the surfaces of flower-like FA20 have attached the largest amount of the Au seeds. As shown in the inset of figure 5(d), the Fe_3O_4–Au MNPs are fully collected by a magnet within 20 s, indicating that Fe_3O_4–Au MNPs show a rapid reaction under the magnetic fields.

Figure S5 presents the zero-field-cooled (ZFC) and field-cooled (FC) magnetization curves of flower-like Fe_3O_4 nanocrystals and the flower-like FA20 (applied filed: 1000 Oe; temperature: 10–300 K). When the temperature increases, the FC magnetization curves monotonically decrease. Moreover, ZFC curves of flower-like Fe_3O_4 nanocrystals and flower-like FA20 peak at 210 and 197 K, respectively, corresponding to their blocking temperatures. The slight drop of the blocking temperature after Au seeds deposition may attribute to the impaired dipolar interaction between the magnetic cores [44, 45].

To investigate the catalytic properties of Fe_3O_4–Au MNPs, the as-prepared samples were used to catalyze and degrade RhB with excess $NaBH_4$. The catalytic degradation process of RhB with sheet-like FA20 was detected by UV–vis spectrophotometer, as shown in figure 6(a). The absorption intensity of RhB peaks at 554 nm, and then shows a downward trend before it completely disappears after 16 min In contrast, pure Fe_3O_4 nanocrystals have no catalytic effect on RhB, as shown in figure 6(b) [46]. In other words, Au seeds play a significant role in catalytic reduction of RhB. To help

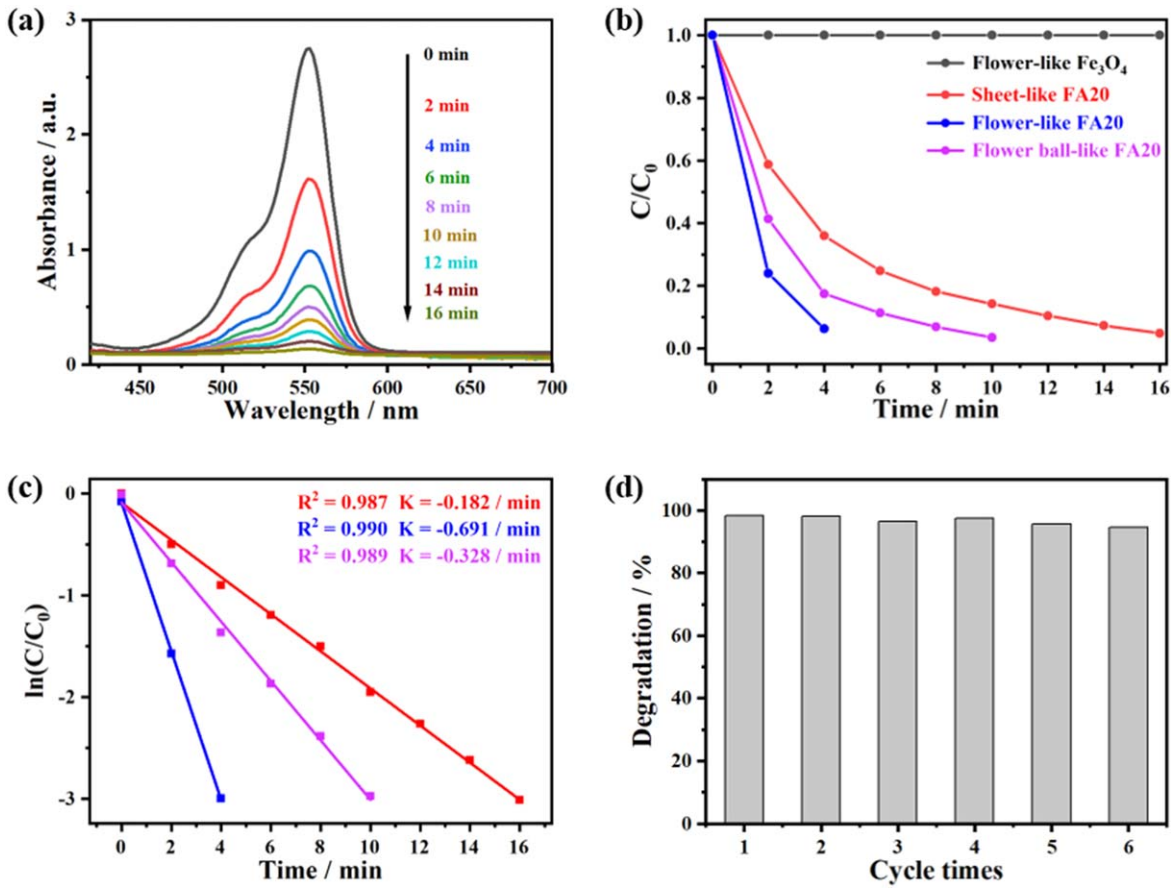

Figure 6. Time-dependent UV–vis absorption spectra of RhB catalyzed by sheet-like FA20 (a), C/C_0 versus reaction time during RhB reduction by flower-like Fe_3O_4 nanocrystals, sheet-like FA20, flower-like FA20 and flower ball-like FA20 (b), ln(C/C_0) versus reaction time during RhB reduction by sheet-like FA20, flower-like FA20 and flower ball-like FA20 (c) and the recyclability of flower-like FA20 for the catalytic reduction of RhB (d).

better understand the catalytic process, the below mechanism is proposed: As is well known, RhB is electrophilic and BH_4^- ions are nucleophiles A nucleophile tend to donate electrons to the metal nanocrystals while an electrophile can capture electrons from the metal nanocrystals. When the BH_4^- ions and RhB molecules are absorbed on the surfaces of the Fe_3O_4–Au MNPs, the electrons are transferred from BH_4^- ions to RhB via Au seeds [47]. As seen in figure 6(b) and figure S6, it only takes 4 min to degrade RhB by flower-like FA20. In comparison, sheet-like and flower ball-like FA20 need 16 min and 10 min, respectively. As illustrated in figure 6(c), the reaction rate constant of the flower-like FA20 is 0.691 min^{-1}, which is 3.8 and 2.1 times higher than that of the sheet-like and flower ball-like FA20, obtained via the equation ln $(C_t/C_0) = -kt$, where C_t is the concentration of RhB at reaction time t, C_0 is the initial concentration of RhB at $t = 0$ and k is the rate constant [48]. Therefore it's safe to say, flower-like FA20 has the highest catalytic activity at room temperature. The same process was later repeated for six times, and the catalytic activities of the flower-like FA20 remained almost unchanged, as shown in figure 6(d). It indicates that flower-like FA20 has excellent recyclability and a stable conversion efficiency of around 96.7%.

The above results show that under the same experimental conditions, more Au seeds are deposited onto the flower-like Fe_3O_4 nanocrystals surfaces than the sheet-like and the flower ball-like Fe_3O_4 nanocrystals surfaces. It can be confirmed that the flower-like Fe_3O_4 nanocrystals have larger specific surface area than the sheet-like and the flower ball-like Fe_3O_4 nanocrystals, and thus can provide the largest sites to deposit Au seeds. To gain a better understanding about how the amount of Au seeds affects the catalytic performance, we adjusted the amount of Au seeds loaded on the surfaces of the flower-like Fe_3O_4 nanocrystals. As it can be seen in figure 7(a), the XRD peak intensity of Au increases when the amount of Au seeds increases. And as shown in figure S7, no impurities are observed except for Fe, Au, O, and C. As illustrated in figure 7(b) and (c), the Fe 2*p* peak positions move to lower binding energies, and the Au 4*f* peak positions move to higher binding energies when the amount of Au seeds increases, due to the strengthening of the electronic interaction between Au and Fe_3O_4. As shown in figure 7(d) and (e), the SPR absorption peak of Au exhibits a red shift and the *Ms* value deceases when the amount of Au seeds increases.

To test the catalytic performance of Fe_3O_4–Au MNPs, 4-NP was chosen as a target pollutant. As shown in figure S8,

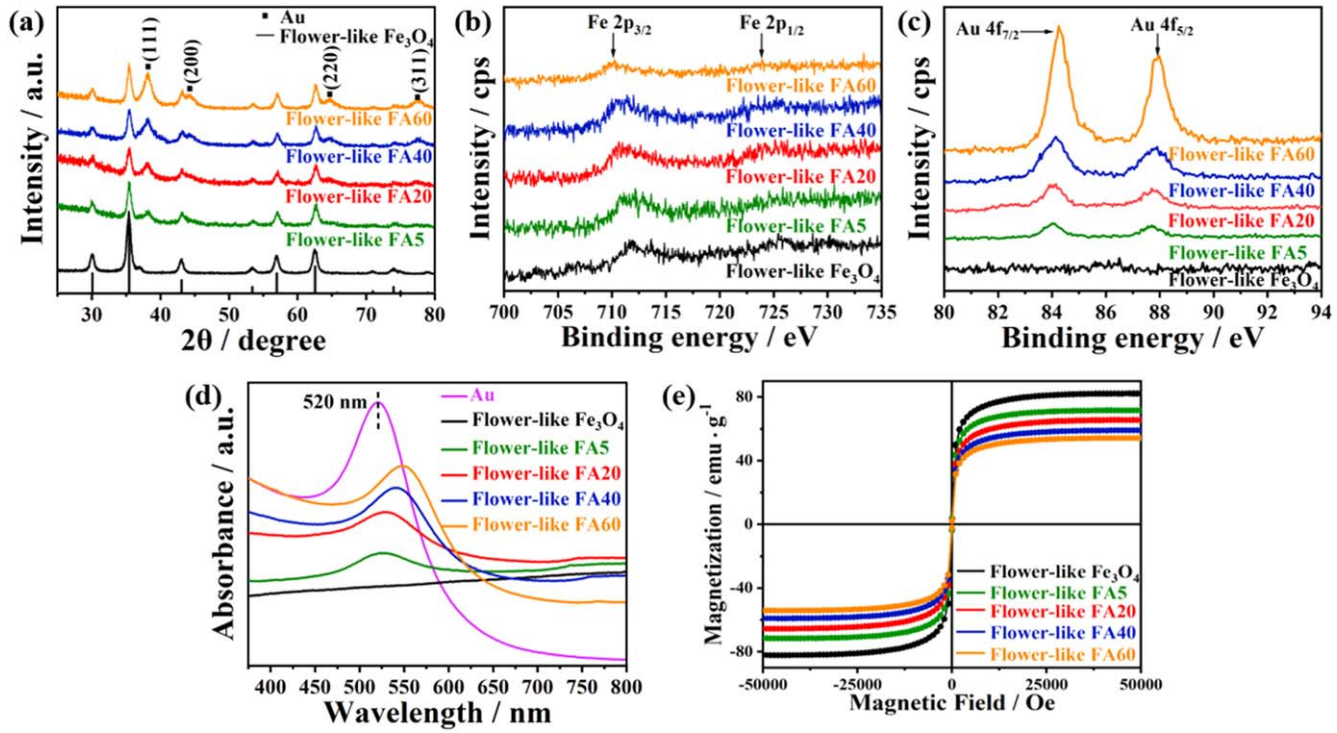

Figure 7. XRD patterns (a), high-resolution XPS scans of Fe *2p* (b) and Au *4 f* (c), UV–vis spectra (d) and *M-H* loops (e) of as-prepared flower-like Fe_3O_4 nanocrystals, flower-like FA5, flower-like FA20, flower-like FA40 and flower-like FA60.

the absorption peak of 4-NP at 317 nm shifts to 400 nm when the $NaBH_4$ is added, because of the conversion of 4-NP [49, 50]. Figure 8(a) shows the time-dependent UV–vis absorption spectra of 4-NP catalyzed by the flower-like FA5 with the presence of $NaBH_4$. Due to the degradation of 4-NP, the peak spectra intensity decreases with the reaction time. Later, 4-aminopyridine (4-AP) is generated and a new peak is formed at 300 nm, which demonstrates that Fe_3O_4–Au MNPs can converse 4-NP to 4-AP [51, 52]. 34 min after reaction, the absorption peak disappears completely. The photograph of 4-NP with the reaction time is shown in figure S9. Figures 8(b) and (c) demonstrate the linear relation between $\ln(C/C_0)$ and t for reducing 4-NP with flower-like FA5, flower-like FA20, flower-like FA40 and flower-like FA60. In comparison, figure 8(b) shows that the degradation cannot take place when pure flower-like Fe_3O_4 nanocrystals are employed. The above results further confirm that Au seeds play an essential role in catalyzing 4-NP and the rate constant is directly proportional to the amount of Au seeds. The catalytic performances of the flower-like FA20 remain almost unchanged after recycling, as shown in figure 8(d).

Though we have proved that the degradation efficiency of the flower-like Fe_3O_4–Au MNPs could be enhanced by increasing the amount of Au seeds, we still need to investigate the relationship between the amount of Au seeds and TOF, which is also a crucial indicator of the catalytic performance. Therefore, the TOF values of the 4-NP reduction by flower-like FA5, flower-like FA20, flower-like FA40 and flower-like FA60 were studied and summarized in Table 1, which were 10.14, 9.58, 10.78 and 9.58 min^{-1}, respectively. From which we can conclude that flower-like FA40 were preferred due to its high degradation efficiency and TOF value.

4. Conclusions

In summary, we reported the tailored design of highly efficient and recyclable Fe_3O_4–Au magnetic nanocomposite (MNP) catalysts. First, Fe_3O_4 nanocrystals with sheet-like, flower-like and flower ball-like morphologies were developed via engineered amounts of urea. As revealed by the investigation, urea played an important part in the formation of iron alkoxide precursors, based on which the possible growth mechanism was proposed. When 90 mmol urea was added, the Fe_3O_4 nanocrystals exhibited 3D flower-like shape with the BET specific surface area of 60.73 $m^2 g^{-1}$. Then, Fe_3O_4–Au MNPs with strong magnetic responsiveness were obtained by the seed deposition method. With the presence of $NaBH_4$, the catalytic ability of Fe_3O_4–Au MNPs with different morphologies was compared by degrading RhB and 4-NP. It was found that the catalytic reduction obeyed the pseudo-first order kinetics and the flower-like FA20 had the most desirable catalytic effect, with a record high degradation efficiency of 96.7%. When we further tune the amount of Au seeds from 5 mL to 60 mL, we found that the degradation efficiency of the flower-like Fe_3O_4–Au MNPs was improved with the increase of Au seeds, but the TOF value reached a peak of 10.78 min^{-1} when 40 ml Au seeds were added, which gave us the most cost-effective amount of Au seeds. We also proved that the catalytic ability of the proposed Fe_3O_4–Au MNPs were almost unchanged after recycling. Our study

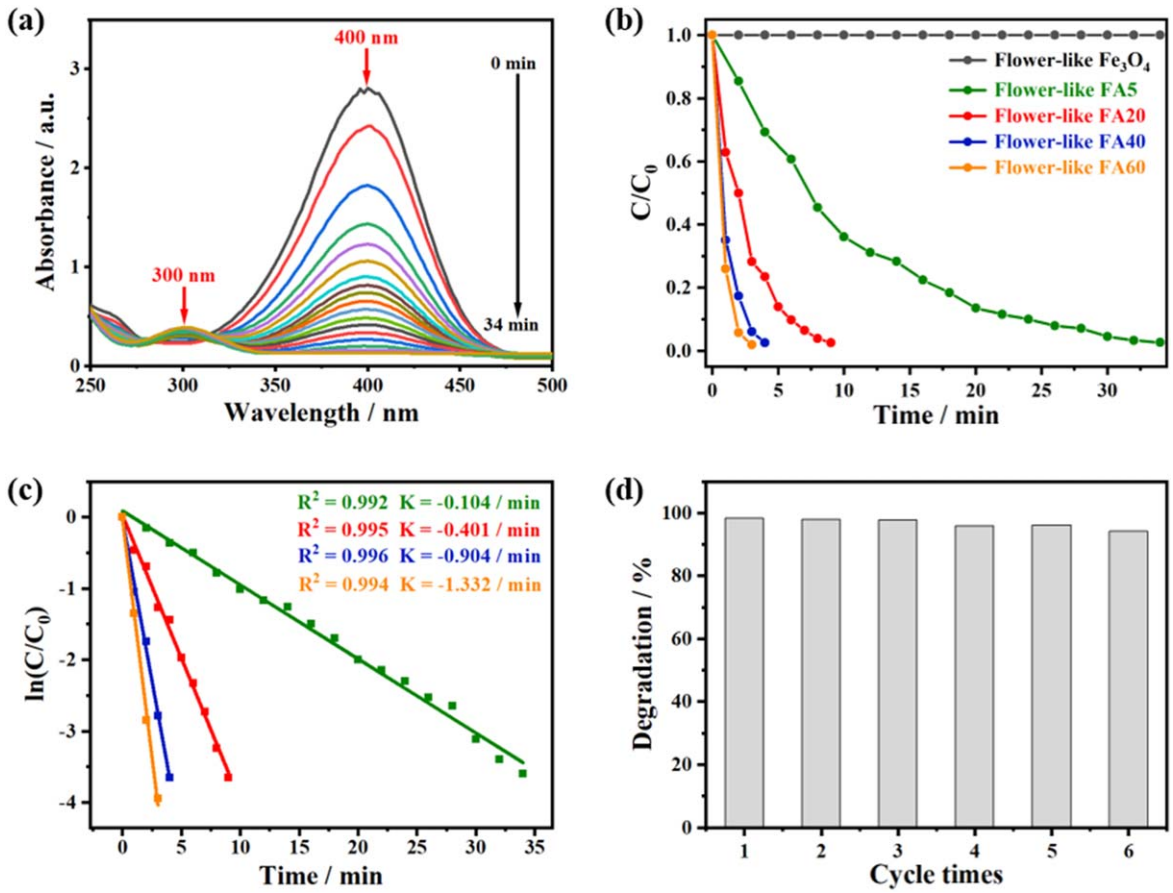

Figure 8. Time-dependent UV–vis absorption spectra of 4-NP catalyzed by flower-like FA5 (a), C/C_0 versus reaction time during 4-NP reduction by flower-like Fe_3O_4 nanocrystals, flower-like FA5, flower-like FA20, flower-like FA40 and flower-like FA60 (b), $\ln(C/C_0)$ versus reaction time during 4-NP reduction by flower-like FA5, flower-like FA20, flower-like FA40 and flower-like FA60 (c) and the recyclability of flower-like FA20 for the catalytic reduction of 4-NP (d).

Table 1. Comparison of catalytic capacities of various catalysts for 4-NP.

Catalyst	Kinetic rate constant (k) (min^{-1})	TOF[a] (min^{-1})
Flower-like FA5	0.104	10.14
Flower-like FA20	0.401	9.58
Flower-like FA40	0.904	10.78
Flower-like FA60	1.332	9.58

[a] Turnover frequency (TOF) = (moles of the reacted organic substrate/moles of noble metal)×reaction time (min^{-1}).

sheds the light into the tailored design of highly efficient and recyclable catalysts for RhB and 4-NP and can promisingly enhance the water pollution treatment.

Acknowledgments

This research was funded by the National Natural Science Foundation of China (Grant Numbers 21676115, 51609100, 61675090, 61575080 and 61705020).

ORCID iDs

Jinghai Yang https://orcid.org/0000-0001-8409-6035
Yang Liu https://orcid.org/0000-0003-1485-8764

References

[1] Danish M and Ahmad T 2018 A review on utilization of wood biomass as a sustainable precursor for activated carbon production and application *Renew. Sust. Energ. Rev.* **87** 1–21
[2] Veisi H, Razeghi S, Mohammadi P and Hemmati S 2019 Silver nanoparticles decorated on thiol-modified magnetite nanoparticles (Fe_3O_4/SiO_2–Pr–S–Ag) as a recyclable nanocatalyst for degradation of organic dyes *Mater. Sci. Eng.* C **97** 624–31
[3] Ismail M, Khan M I, Khan S B, Khan M A, Akhtar K and Asiri A M 2018 Green synthesis of plant supported Cu–Ag and Cu–Ni bimetallic nanoparticles in the reduction of nitrophenols and organic dyes for water treatment *J. Mol. Liq.* **260** 78–91
[4] Zhang Y M, Yuan S, Day G, Wang X, Yang X Y and Zhou H C 2018 Luminescent sensors based on metal-organic frameworks *Coordin. Chem. Rev.* **354** 28–45
[5] Bordbar M, Negahdar N and Nasrollahzadeh M 2018 Melissa Officinalis L. leaf extract assisted green synthesis of CuO/

ZnO nanocomposite for the reduction of 4-nitrophenol and Rhodamine B *Sep. Purif. Technol.* **191** 295–300
[6] Le X D, Dong Z P, Liu Y S, Jin Z C, Huy T D, Le M and Ma J T 2014 Palladium nanoparticles immobilized on core–shell magnetic fibers as a highly efficient and recyclable heterogeneous catalyst for the reduction of 4-nitrophenol and Suzuki coupling reactions *J. Math. Chem.* A **2** 19696–706
[7] Moscoso R, Barrientos C, Moris S and Squella J A 2019 Electrocatalytic oxidation of NADH in a new nanostructured interface with an entrapped butylpyrene nitroaromatic derivative *J. Electroanal. Chem.* **837** 48–54
[8] Hui M, Yan P S, Qi H Y, Xin Z R, Anatoly Z and Wei C 2018 A highly efficient magnetic chitosan 'fluid' adsorbent with a high capacity & fast adsorption kinetics for dyeing wastewater purification *Chem. Eng. J.* **345** 556–65
[9] Mishra D D and Tan G L 2018 Visible photocatalytic degradation of methylene blue on magnetic $SrFe_{12}O_{19}$ *J. Phys. Chem. Solids* **123** 157–61
[10] Guo S, Wang Y X, Zhang F, Gao R X, Liu M M, Dong L R, Liu Y, Zhang Y J and Chen L 2018 *In Situ* synthesis of Ag@Cu_2O-rGO architecture for strong light–matter Interactions *Nanomaterials* **8** 444
[11] Peng Y, Lu B Z and Chen S W 2018 Carbon-supported single atom catalysts for electrochemical energy conversion and storage *Adv. Mater.* **30** e1801995
[12] Babu B, Koutavarapu R, Harish V V N, Shim J and Yoo K 2019 Novel *in situ* synthesis of Au/SnO_2 quantum dots for enhanced visible-light-driven photocatalytic applications *Ceram. Int.* **45** 5743–50
[13] Yu X L, Diao Q, Zhang X K, Lee Y and Liu H G 2017 *In situ* generated Pb nanoclusters on basic lead carbonate ultrathin nanoplates as an effective heterogeneous catalyst *CrystEngComm* **19** 2860–9
[14] Linnenbank H, Grynko Y, Forstner J and Linden S 2016 Second harmonic generation spectroscopy on hybrid plasmonic/dielectric nanoantennas *Light-Sci. Appl.* **5** e16013
[15] Shan H Y *et al* 2019 Direct observation of ultrafast plasmonic hot electron transfer in the strong coupling regime *Light-Sci. Appl.* **8** 9
[16] Liu F, Liu X, Astruc D and Gu H 2019 Dendronized triazolyl-containing ferrocenyl polymers as stabilizers of gold nanoparticles for recyclable two-phase reduction of 4-nitrophenol *J. Colloid Interface Sci.* **533** 161–70
[17] Chen L, Liu M M, Zhao Y, Kou Q W, Wang Y X, Liu Y, Zhang Y J, Yang J H and Jung Y M 2018 Enhanced catalyst activity by decorating of Au on Ag@Cu_2O nanoshell *Appl. Surf. Sci.* **435** 72–8
[18] Ilgin P, Ozay O and Ozay H 2019 A novel hydrogel containing thioether group as selective support material for preparation of gold nanoparticles: synthesis and catalytic applications *Appl. Catal.* B **241** 415–23
[19] Fang Q L, Zhang J F, Bai L F, Duan J Y, Xu H J, Cham-Fai Leung K and Xuan S H 2019 *In situ* redox-oxidation polymerization for magnetic core–shell nanostructure with polydopamine-encapsulated-Au hybrid shell *J. Hazard. Mater.* **367** 15–25
[20] Dauthal P and Mukhopadhyay M 2012 Prunus domestica fruit extract-mediated synthesis of gold nanoparticles and its catalytic activity for 4-nitrophenol reduction *Ind. Eng. Chem. Res.* **51** 13014–20
[21] Chen X, Chen X, Cai S C, Chen J, Xu W J, Jia H P and Chen J 2017 Catalytic combustion of toluene over mesoporous Cr_2O_3-supported platinum catalysts prepared by *in situ* pyrolysis of MOFs *Chem. Eng. J.* **334** 768–79
[22] Chen Y *et al* 2018 Enhanced catalytic reduction of 4-nitrophenol driven by Fe_3O_4–Au magnetic nanocomposite interface engineering: from facile preparation to recyclable application *Nanomaterials* **8** 353
[23] Liu Y, Kou Q W, Wang D D, Chen L, Sun Y T, Lu Z Y, Zhang Y Y, Wang Y X, Yang J H and Xing S G Z 2017 Rational synthesis and tailored optical and magnetic characteristics of Fe_3O_4–Au composite nanoparticles *J. Mater. Sci.* **52** 10163–74
[24] Jung Y, Son Y H and Lee J K 2012 3D self-assembly of flower-like particles via microwave irradiation for water treatment *RSC Adv.* **2** 5877
[25] Prabhakaran T, Mangalaraja R V, Denardin J C and Varaprasad K 2018 The effect of capping agents on the structural and magnetic properties of cobalt ferrite nanoparticles *J. Mater. Sci.—Mater. Electron.* **29** 11774–82
[26] Nasrollahzadeh M, Sajjadi M and Khonakdar H A 2018 Synthesis and characterization of novel Cu(II) complex coated Fe_3O_4@SiO_2 nanoparticles for catalytic performance *J. Mol. Struct.* **1161** 453–63
[27] Li J, Tan L, Wang G and Yang M 2015 Synthesis of double-shelled sea urchin-like yolk-shell Fe_3O_4/TiO_2/Au microspheres and their catalytic applications *Nanotechnology* **26** 095601
[28] Shevchenko E V, Bodnarchuk M I, Kovalenko M V, Talapin D V, Smith R K, Aloni S, Heiss W and Alivisatos A P 2008 Gold/iron oxide core/hollow-shell nanoparticles *Adv. Mater.* **20** 4323–9
[29] Yang J H *et al* 2017 Effects of amount of benzyl ether and reaction time on the shape and magnetic properties of Fe_3O_4 nanocrystals *Powder Technol.* **319** 53–9
[30] Liu Y, Zhang Y Y, Kou Q W, Chen Y, Han D L, Wang D D, Lu Z Y, Chen L, Yang J H and Xing S 2018 Eco-friendly seeded Fe_3O_4-Ag nanocrystals: a new type of highly efficient and low cost catalyst for methylene blue reduction *RSC Adv.* **8** 2209–18
[31] Kadam A N, Moniruzzaman M and Lee S-W 2019 Dual functional S-doped g-C_3N_4 pinhole porous nanosheets for selective fluorescence sensing of Ag^+ and visible-light photocatalysis of dyes *Molecules* **24** 450
[32] Baskakov A O, Solov'eva A Y, Ioni Y V, Starchikov S S, Lyubutin I S, Khodos I I, Avilov A S and Gubin S P 2017 Magnetic and interface properties of the core–shell Fe_3O_4/Au nanocomposites *Appl. Surf. Sci.* **422** 638–44
[33] Chen H M, Li Y L, Wu H, Sun N R and Deng C H 2019 Smart hydrophilic modification of magnetic mesoporous silica with zwitterionic l-cysteine for endogenous glycopeptides recognition *ACS Sustain Chem. Eng.* **7** 2844–51
[34] Wang N, Zhang M, Liu L B, Zheng J, Xu J L, Hayat T and Alharbi N S 2019 Space-confined pyrolysis for fabrication of peacods-like Fe_3O_4@C-Ni nanostructures for catalysis and protein adsorption *Nanotechnology* **30** 415602
[35] Klyushin A Y, Rocha T C, Havecker M, Knop-Gericke A and Schlogl R 2014 A near ambient pressure XPS study of Au oxidation *Phys. Chem. Chem. Phys.* **16** 7881–6
[36] Wang D J, Jin Y, Park C M, Heo J Y, Bai X, Aich N and Su C M 2018 Modeling the transport of the 'new-horizon' reduced graphene oxide-metal oxide nanohybrids in water-saturated porous media *Environ. Sci. Technol.* **52** 4610–22
[37] Liz-Marzán L M, Giersig M and Mulvaney P 1996 Synthesis of nanosized gold-silica core–shell particles *Langmuir* **12** 4329–35
[38] Zhang F, Guo S, Liu Y, Chen L, Wang Y X, Gao R X, Zhu A N, Zhang X L and Zhang Y J 2018 Controlling the 3D electromagnetic coupling in co-sputtered Ag–SiO_2 nanomace arrays by lateral sizes *Nanomaterials* **8** 493
[39] Schick I, Gehrig D, Montigny M, Balke B, Panthöfer M, Henkel A, Laquai F and Tremel W 2015 Effect of charge transfer in magnetic-plasmonic Au@MO_x (M = Mn, Fe) heterodimers on the kinetics of nanocrystal formation *Chem. Mater.* **27** 4877–84

[40] Dong H, Dai Y, Zhang X J, Zhang Z G, Fu S L and Zhong Z L 2018 The influence of amine structures on the stability and catalytic activity of gold nanoparticles stabilized by amine-modified hyperbranched polymers *Nanotechnology* **29** 055705

[41] Lou L, Yu K, Zhang Z L, Huang R, Wang Y T and Zhu Z Q 2012 Facile methods for synthesis of core–shell structured and heterostructured Fe_3O_4@Au nanocomposites *Appl. Surf. Sci.* **258** 8521–6

[42] Liu Y *et al* 2018 Fe_3O_4/Au binary nanocrystals: facile synthesis with diverse structure evolution and highly efficient catalytic reduction with cyclability characteristics in 4-nitrophenol *Powder Technol.* **338** 26–35

[43] Lu Z Y, Zhou G S, Song M S, Wang D D, Huo P W, Fan W Q, Dong H J, Tang H, Yan F and Xing G Z 2019 Magnetic functional heterojunction reactors with 3D specific recognition for selective photocatalysis and synergistic photodegradation in binary antibiotic solutions *J. Math. Chem.* A **7** 13986–4000

[44] Freitas M C C, Couto M M S, Barroso M F, Pereira C, delos-Santos-Álvarez N, Miranda-Ordieres A J, Lobo-Castañón M J and Delerue-Matos C 2016 Highly monodisperse Fe_3O_4@Au superparamagnetic nanoparticles as reproducible platform for genosensing genetically modified organisms *ACS Sens.* **1** 1044–53

[45] Salado J, Insausti M, Lezama L, Gil de Muro I, Moros M, Pelaz B, Grazu V, de la Fuente J M and Rojo T 2012 Functionalized Fe_3O_4@Au superparamagnetic nanoparticles: *in vitro* bioactivity *Nanotechnology* **23** 315102

[46] Xie Y M, Lv L, Zhang S J, Pan B C, Wang X S, Chen Q, Zhang W M and Zhang Q X 2011 Fabrication of anion exchanger resin/nano-CdS composite photocatalyst for visible light RhB degradation *Nanotechnology* **22** 305707

[47] Liu Y *et al* 2018 Highly efficient, low-cost, and magnetically recoverable FePt-Ag nanocatalysts: towards green reduction of organic dyes *Nanomaterials* **8** 329

[48] Zhang K H, Wang C W, Rong Z, Xiao R, Zhou Z and Wang S Q 2017 Silver coated magnetic microflowers as efficient and recyclable catalysts for catalytic reduction *New J. Chem.* **41** 14199–208

[49] Panigrahi S, Basu S, Praharaj S, Pande S, Jana S, Pal A, Ghosh S K and Pal T 2007 Synthesis and size-selective catalysis by supported gold nanoparticles: study on heterogeneous and homogeneous catalytic process *J. Phys. Chem.* C **111** 4596–605

[50] Liu Y Y *et al* 2018 High-efficient catalytic reduction of 4-nitrophenol based on reusable Ag nanoparticles/graphene-loading loofah sponge hybrid *Nanotechnology* **29** 315702

[51] Wang S, Niu S Y, Li H S, Lam K K, Wang Z R, Du P Y, Leung C W and Qu S X 2019 Synthesis and controlled morphology of Ni@Ag core–shell nanowires with excellent catalytic efficiency and recyclability *Nanotechnology* **30** 385603

[52] Zhao K, Niu W B, Wang Y P and Zhang S F 2019 Electrophilic substitution reaction as a facile and general approach for reactive removal of native ligands from nanocrystals surface *Nanotechnology* **30** 015701